Lab on a Chip

Accepted Manuscript

This is an *Accepted Manuscript*, which has been through the Royal Society of Chemistry peer review process and has been accepted for publication.

Accepted Manuscripts are published online shortly after acceptance, before technical editing, formatting and proof reading. Using this free service, authors can make their results available to the community, in citable form, before we publish the edited article. We will replace this *Accepted Manuscript* with the edited and formatted *Advance Article* as soon as it is available.

You can find more information about *Accepted Manuscripts* in the **Information for Authors**.

Please note that technical editing may introduce minor changes to the text and/or graphics, which may alter content. The journal's standard **Terms & Conditions** and the **Ethical guidelines** still apply. In no event shall the Royal Society of Chemistry be held responsible for any errors or omissions in this *Accepted Manuscript* or any consequences arising from the use of any information it contains.

Journal Name

ARTICLE TYPE

The importance of travelling wave components in standing surface acoustic wave (SSAW) systems[†]

Citsabehsan Devendran,[a] Thomas Albrecht,[b] Jason Brenker,[a] Tuncay Alan,[a] and Adrian Neild[*a]

The use of ultrasonic fields to manipulate particles, cells and droplets has become widespread in lab on a chip (LOC) systems. There are two dominant actuation methods, the use of bulk acoustic waves (BAW) or surface acoustic waves (SAW). The development of BAW actuated systems have been underpinned by a robust understanding of the link between the ultrasonic field and forces which can be generated. In this work, we examine this link for standing surface acoustic waves (SSAW) comparing the relative strengths of streaming induced drag and acoustic radiation forces on suspended particles. To achieve this we have employed boundary conditions which accurately capture the travelling wave components of the pseudo-standing wave field, describe the key features of the acoustic radiation force fields and the acoustic streaming fields which can be generated, and finally we show that the relative importance of these two mechanisms is spatially dependant within a fluid chamber. The boundary condition used models the SSAW as two counter-propagating travelling waves, rather than assuming a standing wave directly. This allows the accurate inclusion of energy decay as the SAW couples into the fluid chamber and the resulting travelling wave component. This study shows that this previously neglected complexity of the SAW field is a critical factor in the nature of the resultant streaming field, as it gives rise to strong streaming rolls at the channel walls, which we validate experimentally. These rolls result in spatial variations of the dominant forces which in turn varies particle migration patterns spatially across the fluid domain.

1 Introduction

The concept behind lab-on-a-chip (LOC) systems, is the aim to achieve small, compact, efficient and complete portable systems for various fluid handling applications.[1] One aspect of achieving this is to be able to precisely manipulate suspended matter and fluids at these size-scales. To this end, various passive and active methods have been utilised successfully. Many of these approaches exploit the combination of hydrodynamic forces imposed by the fluid flow profile[2,3] and externally applied forces arising from magnetic,[4,5] optical,[6,7] dielectrophoretic (DEP)[8,9] and acoustophoretic[10–12] fields.

Acoustophoresis[13–15] can be used to manipulate suspended matter (i.e. biological matter or synthetic particles), fluid interfaces or create fluid flows, using acoustic actuation. It

uses actuation methods which can be easily integrated on-chip, can be driven by portable miniaturised circuits[15] and have been shown to have good bio-compatibility[16–18]. Typically, acoustophoretic microfluidic systems are excited using either bulk acoustic waves[19–22] (BAW) or surface acoustic waves[23–28] (SAW). The former excites resonances within the fluid volume coupled from a vibrating structure, whereas, the latter utilises a spatially periodic electrical field to create a resonant condition on a piezoelectric substrate. In the case of SAW, a further distinction can be made between travelling SAWs (TSAWs), whereby a single wave propagates through the system and standing SAWs (SSAWs), where, two counter-propagating travelling waves interfere with each other to establish a pseudo-standing wave field within the fluid domain.

Suspended particles within a fluid volume subjected to an incident acoustic wave experience two main forces, namely the acoustic radiation force[29,30] (ARF) and acoustic streaming induced drag forces,[31,32] these have been used individually to manipulate suspended matter via ARF[10] and acoustic streaming fields[33] as well as in combination.[34,35] Whilst BAW systems have been extensively studied theoretically and numerically,[36–40] com-

[a] Laboratory for Micro Systems, Department of Mechanical and Aerospace Engineering, Monash University, Clayton, Victoria 3800, Australia.; E-mail: adrian.neild@monash.edu
[b] Department of Mechanical and Aerospace Engineering, Monash University, Clayton, Victoria 3800, Australia.
† Electronic Supplementary Information (ESI) available: [details of any supplementary information available should be included here]. See DOI: 10.1039/b000000x/

parable studies describing the acoustic forces and streaming fields in SAW-based systems are rather limited. Nama *et al*[41] have reported a numerical study of streaming, however, this is limited to a single wavelength wide microchannel. It demonstrates an important difference between streaming in BAW and SAW generated sound fields with regard to how the fluid boundary region drives the acoustic streaming; in a BAW field the sound propagation is parallel to the edge of the fluid chamber giving rise to strong boundary effects[38], whilst these are lessened in a SAW field in which sound propagates at an angle to the boundary. However, the study was limited to a single wavelength, and as such the boundary conditions used do not accurately capture the travelling wave components within a SSAW. These become important in larger systems arising from the attenuation of SAW as they propagate along the substrate-fluid interface due to energy transfer into the fluid domain. The local mismatch in the amplitudes of the two counter-propagating SAWs caused by this attenuation gives rise to TSAW components in what is usually nominally considered to be a standing wave. Recently, Devendran *et al*[42] has exaggerated this phenomenon by applying asymmetrical power to opposing inter-digital transducers (IDTs) exploiting the combination of TSAWs and SSAWs to achieve enhanced particle sorting within a static fluid system.

Here, we derive suitable boundary conditions to numerically model a SAW-driven system accommodating for the inherent travelling wave components. This allows the accurate investigation of acoustophoretic motion of particles within systems that span multiple wavelengths, in line with most SSAW based systems developed.[43–47] We employ perturbation theory as used in previous studies for BAW[38,48] systems, whereby the first-order solution are used to calculate the time-averaged pressure field and steady-state acoustic streaming fields, that give rise to ARF and acoustic streaming induced drag forces respectively. Using this approach, combined with accurate boundary conditions, the existence of some key features are identified: a) acoustic nearfield lobing effects, b) the accurate description of the presence of an anechoic corner[49] close to the channel wall boundary , c) the resulting large streaming rolls which dominate the streaming profile, d) a spatial dependence across the fluid chamber on whether acoustic streaming or acoustic radiation force dominates particle migration patterns and e) an increase in the dominance of streaming with increasing chamber heights.

2 Governing equation

Employing perturbation theory,[48] we let

$$P = P_0 + \varepsilon P_1 + \varepsilon^2 P_2 \tag{1a}$$

$$\rho = \rho_0 + \varepsilon \rho_1 + \varepsilon^2 \rho_2 \tag{1b}$$

$$\boldsymbol{v} = \boldsymbol{v}_0 + \varepsilon \boldsymbol{v}_1 + \varepsilon^2 \boldsymbol{v}_2 \tag{1c}$$

where, ε is a non-dimensional small parameter.

The pressure, $P_1 = \rho_1 c_0^2$ is given by the (isentropic) derivative

$c_0^2 = (\partial P/\partial \rho)_s$. Subscripts 0, 1 and 2 denote the order of the expression (i.e. initial, first and second-order) and ρ is the density. It should be noted that v_0 is assumed to be zero (i.e. $v_0 = 0$ m/s), given the absence of an initial flow.

If we consider the thermodynamic equation of state by expressing P in terms of the density ρ (Equation 2a), the continuity equation for density (Equation 2b) and the Navier-Stokes equation for the velocity field v (Equation 2c), we have

$$P = P(\rho) \tag{2a}$$

$$\frac{\partial \rho}{\partial t} = -\nabla \cdot (\rho \boldsymbol{v}) \tag{2b}$$

$$\rho \frac{\partial \boldsymbol{v}}{\partial t} = -\nabla P - \rho (\boldsymbol{v} \cdot \nabla) \boldsymbol{v} + \eta \nabla^2 \boldsymbol{v} + \beta \eta \nabla (\nabla \cdot \boldsymbol{v}) \tag{2c}$$

where, η is the dynamic viscosity and β is the viscosity ratio.

The first-order terms of the governing equation in Equation 2b and 2c are given as,

$$\frac{\partial \rho_1}{\partial t} = -\rho_0 \nabla \cdot \boldsymbol{v}_1 \tag{3a}$$

$$\rho_0 \frac{\partial \boldsymbol{v}_1}{\partial t} = -\nabla P_1 + \eta \nabla^2 \boldsymbol{v}_1 + \beta \eta \nabla (\nabla \cdot \boldsymbol{v}_1) \tag{3b}$$

Typically, the second-order fields are negligible when compared to the first-order fields. However, as the first-order fields are harmonic, they time-average (denoted by the angled brackets) to zero over an oscillation cycle, $\langle A \sin (\omega t) \rangle = 0$, where A is the amplitude of oscillation.

However, second-order terms, in which two time harmonic terms are multiplied together, time-average to non-zero values, $\langle B \sin^2 (\omega t) \rangle = B/2$, therefore, the second-order terms need to be considered. As such, Equation 2b and 2c become

$$\nabla \langle \rho_1 \boldsymbol{v}_1 \rangle = -\rho_0 \nabla \cdot \boldsymbol{v}_2 \tag{4a}$$

$$\langle \rho_1 \frac{\partial \boldsymbol{v}_1}{\partial t} \rangle + \rho_0 \langle (\boldsymbol{v}_1 \cdot \nabla) \boldsymbol{v}_1 \rangle = -\nabla \langle P_2 \rangle + \eta \nabla^2 \boldsymbol{v}_2 + \beta \eta \nabla (\nabla \cdot \boldsymbol{v}_2) \tag{4b}$$

3 Time-averaged acoustic forces

We now calculate the time-averaged forces acting on a single suspended particle. The relevant forces are the acoustic radiation forces $\boldsymbol{F}_{ARF}$ and the Stokes drag forces $\boldsymbol{F}_{drag}$ arising from acoustic streaming fields.

If we consider a particle of radius a much smaller than the wavelength λ (i.e. $a \ll \lambda$), the radiation force takes the form:[50]

$$\boldsymbol{F}_{ARF} = -\pi a^3 \left[\frac{2\kappa_0}{3} \mathbb{R} \left[f_1^* P_1^* \nabla P_1 \right] - \rho_0 \mathbb{R} \left[f_2^* \boldsymbol{v}_1^* \cdot \nabla \boldsymbol{v}_1 \right] \right] \tag{5}$$

where, $\kappa_0 = 1/(\rho_0 c_0^2)$ is the compressibility of the fluid domain, $\mathbb{R}[A]$ denotes the real part of quantity A, the asterisk denotes complex conjugates of the quantity and factors f_1 and f_2 are given by

$$f_1 = 1 - \frac{\kappa_p}{\kappa_0} \tag{6a}$$

and

$$f_2 = \frac{2(1-\gamma)(\rho_p - \rho_0)}{2\rho_p + \rho_0(1-3\gamma)} \tag{6b}$$

where,

$$\gamma = -\frac{3}{2}\left[1 + i\left(1 + \tilde{\delta}_v\right)\right]\tilde{\delta}_v \tag{7a}$$

$$\tilde{\delta}_v = \frac{\delta_v}{a} \ , \ \delta_v = \sqrt{\frac{2\eta}{\omega\rho_0}} \tag{7b}$$

where, κ_p is the compressibility of the particle, δ_v is the viscous boundary layer thickness and ω is the angular frequency of excitation.

We note that the use of this general equation for ARF, Equation 5, means that no assumption is made as to whether the particles are subjected to a travelling or standing wave, a condition which is required by this study.

Secondly, the Stokes drag experienced by the suspended particle arising from acoustic streaming effects must be considered. A spherical particle is assumed to be subjected to a drag force proportional to the difference between the particle's velocity v_p and the streaming field velocity v_2 (i.e. $v_p - v_2$). We assume the presence of the particle does not affect the streaming field as it migrates. If we neglect wall effects, the drag force F_{drag} can be estimated using the Stokes drag formula

$$F_{drag} = 6\pi\eta a\left(v_2 - v_p\right) \tag{8}$$

In order to express the unknown second-order streaming velocity field v_2 in terms of the known first-order terms, we employ the approach used by Nyborg[51] to equate the governing equation in Equation 2b and 2c to a body force F. The body force F, can be expressed in two terms, F_0 and $F_{Reynolds}$,[52]

$$F_0 - F_{Reynolds} = \frac{\partial(\rho v)}{\partial t} + \rho(v \cdot \nabla)v + v\nabla \cdot \rho v \tag{9a}$$

$$F_0 = \frac{\partial(\rho v)}{\partial t} \tag{9b}$$

$$-F_{Reynolds} = \rho(v \cdot \nabla)v + v\nabla \cdot \rho v \tag{9c}$$

Here, once again we employ the perturbation approach with small disturbances similar to that in Equation 1, also accommodating for the time-average terms as previously demonstrated. It should be noted that, F_0 time-averages to zero in steady state and therefore, $F = -F_{Reynolds}$. Thus, we arrive at the time-independent second-order equations

$$\langle F \rangle = \langle \rho_0(v_1 \cdot \nabla)v_1 + v_1\nabla \cdot \rho_0 v_1 \rangle$$
$$= \rho_0\langle(v_1 \cdot \nabla)v_1 + v_1\nabla \cdot v_1 \rangle \tag{10a}$$

$$\langle F \rangle = -\nabla\langle P_2 \rangle + \beta\eta\nabla(\nabla \cdot v_2) + \eta\nabla^2 v_2 \tag{10b}$$

From the known first-order velocity and pressure fields, we can calculate the Reynolds stress (Equation 10a), which eventually drives the steady acoustic streaming field, accommodating for viscous effects within the fluid domain. This is equivalent to Lighthill's formulation[53] which is used to find the steady acoustic streaming field. Based on Equation 10b, we are able to evaluate the second-order steady state velocity field (i.e. acoustic stream-

ing velocity) v_2, based on the known first-order velocity and pressure fields, accommodating for viscous effects within the fluid domain.

4 Method

4.1 Numerical model

SAW based acoustofluidic devices usually consist of a 128° Y-cut X-propagating Lithium Niobate (LiNbO$_3$: LN) piezoelectric crystal patterned with interdigital transducers (IDTs) which is bonded to PDMS embedded microchannels. To generate a SSAW, two opposing pairs of IDTs are excited with a harmonic A/C signal corresponding to the designed frequency f, resulting in two counter-propagating travelling SAWs along the piezoelectric substrate. A complete model of the physical system would require the consideration of electrostatic, elastic and hydrodynamic effects on the system.[41,54] As such, it would be computationally expensive, restricting models to be relatively small. Modelling full 3-dimensional systems would be extremely demanding and likely require the use of supercomputers. Thus, here we propose a system that consists of the 2-dimensional fluid domain solely. The PDMS walls are replaced using an appropriate impedance boundary condition, (this assumes that the thickness of the PDMS wall exceeds the attenuation length) and the piezoelectric-fluid interface is substituted with a velocity boundary condition as discussed in Section 4.1.1. The computational domain consists of a rectangular water-filled chamber as shown in Fig. 1. The fluid channel dimensions are varied to have a certain width W, and height h, to investigate the effect it has on the resultant pressure and streaming fields. The variables and parameters used in this study are listed in Table 1.

4.1.1 Boundary condition

To obtain an appropriate velocity boundary condition for the bottom fluid boundary (i.e. the LN-fluid interface in Fig. 1 (a)), we start with a displacement profile of the x and y-components imposed by the SAW, which is similar to two counter-propagating travelling waves with the x-component shifted by a phase of $\pi/2$
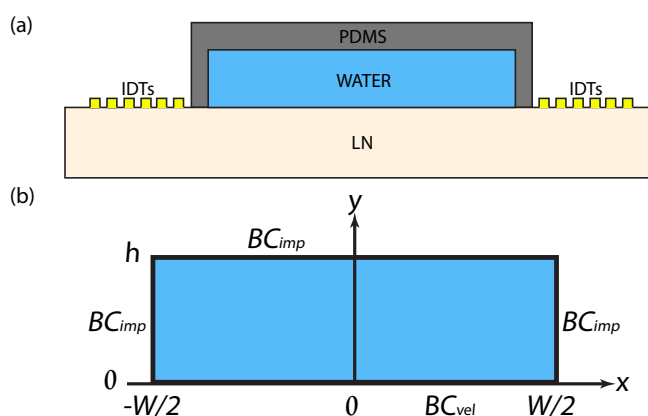
Fig. 1 (a) Cross-sectional sketch of a typical SSAW driven acoustofluidic systems with PDMS bounded microchannels. (b) Sketch of the computational domain with a given width, W and height, h, along with acoustic impedance boundaries, BC_{imp} and velocity boundary condition, BC_{vel}.

and is given in Equation 11. We note, in order to reveal the accurate resultant SAW induced pressure and streaming fields arising from the travelling wave components, the decay coefficient, C_d should be applied to each wave individually. Furthermore, it should be noted that the displacement profile should be expressed in Euler notation (exponential functions) to retain the phase information needed to observe the travelling wave components. Finally, the Y-component of the leftward-propagating wave, d_y should consist of an opposite sign to the rightward-propagating wave in order to accurately capture the elliptical motion of the SAW; whereby, the rotation should be in the opposite direction of propagation (i.e. clockwise when rightward propagating and anti-clockwise when leftward propagating).

$$d_x(x,t) = \zeta d_0 \left[e^{-C_d\left(\frac{W}{2}-x\right)} e^{i\left[-k\left(\frac{W}{2}-x\right)+\omega t\right]} \right.$$

$$\left. + e^{-C_d\left(\frac{W}{2}+x\right)} e^{i\left[k\left(\frac{W}{2}-x\right)+\omega t\right]} \right] \quad (11a)$$

Table 1 Parameters used in numerical simulations (Material properties are at $T = 25°C$).

Water		
Density[55]	ρ_0	997 kg m^{-3}
Speed of sound[55]	c_0	1497 m s^{-1}
Shear viscosity[55]	η	0.890 mPa s
Bulk viscosity[38]	η_b	2.47 mPa s
Compressibility[38]	κ_0	448 TPa^{-1}
Viscous boundary layer (@ 99.85 MHz)[a]	δ_v	53.35 nm
Thermal conductivity[38]	k_{th}	0.603 W m^{-1} K^{-1}
Specific heat capacity[38]	C_p	4183 J kg^{-1} K^{-1}
Thermal expansion coefficient[38]	α_{th}	2.97×10^{-4} K^{-1}
Lithium Niobate (128° YX-cut LiNbO$_3$)		
Speed of sound	c_{LN}	3994 m s^{-1}
Density	ρ_{LN}	4700 kg m^{-3}
Poly-dimethylsiloxane (PDMS; 10:1)		
Density[b]	ρ_{PDMS}	1030 kg m^{-3}
Speed of sound[56]	c_{PDMS}	1076.5 m s^{-1}
Polystyrene		
Density[c]	ρ_p	1050 kg m^{-3}
Speed of sound[41]	c_p	2350 m s^{-1}
Poisson's ratio[41]	σ_p	0.35
Compressibility[d]	κ_p	249 TPa^{-1}
SAW actuation parameters		
SAW wavelength	λ_{SAW}	40 μm
Excitation frequency[e]	f	99.85 MHz
Displacement amplitude	d_0	0.05 nm
Displacement decay coefficient	C_d	2063 m^{-1}

[a] Calculated as $\delta_v = \sqrt{\frac{2\eta}{\rho_0 \omega}}$.

[b] As provided by the supplier product data sheet (Sylgard® 184 Silicone Elastomer).

[c] As provided by the supplier product data sheet (Sigma-Aldrich®).

[d] Calculated as $\kappa_p = \frac{3\left(1-\sigma_p\right)}{1+\sigma_p} \frac{1}{\left(\rho_p c_p^2\right)}$

[e] Calculated as $f = \frac{c_{LN}}{\lambda_{SAW}}$

Note: The PDMS used experimentally consists of a 10:1 mixing ratio (i.e. 10 parts base and 1 part curing agent). The material properties used correspond to this mixing ratio.

$$d_y(x,t) = -d_0 \left[e^{-C_d\left(\frac{W}{2}-x\right)} e^{i\left[-k\left(\frac{W}{2}-x\right)+\omega t-\frac{\pi}{2}\right]} \right.$$

$$\left. - e^{-C_d\left(\frac{W}{2}+x\right)} e^{i\left[k\left(\frac{W}{2}-x\right)+\omega t-\frac{\pi}{2}\right]} \right] \quad (11b)$$

where, ω is the angular frequency of the propagating SAW $\omega = 2\pi f$, f is the excitation frequency, d_0 is the y-displacement amplitude of the SAW, C_d is the SAW attenuation coefficient, $k = 2\pi/\lambda$ is the wavenumber and W is the width of the channel. $\zeta = A_x/A_y =$ is the proportion of the x-component's displacement amplitude A_x as compared to that of y-component.

To comply with the input needed for COMSOL Multiphysics' Thermoacoustic module, we differentiate Equation 11 with respect to time to obtain the velocity boundary condition. For the frequency domain analysis we are conducting, COMSOL Multiphysics accommodates for full harmonic by multiplying the input parameter with a factor of $e^{i\theta}$ where $0 \le \theta \le 2\pi$ is the phase ranging a full harmonic. Therefore, we remove the time-dependent terms after differentiation. The required input velocity boundary condition for each component then reads:

$$\frac{u_x(x,t)}{ie^{i\omega t}} = \zeta d_0 \omega \left[e^{-C_d\left(\frac{W}{2}-x\right)} e^{i\left[-k\left(\frac{W}{2}-x\right)\right]} \right.$$

$$\left. + e^{-C_d\left(\frac{W}{2}+x\right)} e^{i\left[k\left(\frac{W}{2}-x\right)\right]} \right] \quad (12a)$$

$$\frac{u_y(x,t)}{ie^{i\omega t}} = -d_0 \omega \left[e^{-C_d\left(\frac{W}{2}-x\right)} e^{i\left[-k\left(\frac{W}{2}-x\right)-\frac{\pi}{2}\right]} \right.$$

$$\left. - e^{-C_d\left(\frac{W}{2}+x\right)} e^{i\left[k\left(\frac{W}{2}-x\right)-\frac{\pi}{2}\right]} \right] \quad (12b)$$

These boundary conditions have been extensively tested against a numerical model consisting of a 128° Y-cut X-propagating Lithium Niobate (LiNbO$_3$; LN) fully coupled with a fluid domain on its surface. Various channel dimensions, including channel height, channel width and channel wall impedance boundary conditions (i.e. PDMS or water) were investigated to test the consistency of the proposed velocity boundary condition as in Equation 12. The same boundary condition omitting the counter-propagating term can be used to model TSAW systems as well.

In contrast to typical BAW systems that have rigid silicon etched microchannels and are enclosed with hard wall boundary conditions, the boundary conditions for the PDMS channel walls used here (typical in SAW based systems) were modelled with an impedance condition (matched to the acoustic impedance of PDMS (10:1), $Z_{PDMS} = \rho_{PDMS} \times c_{PDMS}$), as used in previous acoustofluidic numerical studies.[41,48] Use of an impedance boundary condition mimics a case of an infinitely thick layer with a specified acoustic impedance. Here, this condition is justified as the typical PDMS wall thickness is significantly thicker than that of the attenuation decay length (at MHz frequencies),[56] thus has minimal reflections of the transmitted wave from the PDMS/air boundary back into the fluid domain. Moreover, all the boundaries are imposed with no-slip boundary conditions $v_{@wall} = 0$

m/s, as used by Muller *et al* and Nama *et al*.[38,41]

4.1.2 Acoustophoretic trajectories

To help visualise the acoustophoretic migration of particles within these fields as a result of ARF and streaming induced drag force, we employ a particle tracking method within COMSOL Multiphysics, similar to that employed in previous studies.[38,41] We consider a dilute suspension (i.e. neglecting particle-particle interactions) of particles that are homogeneously dispersed within the fluid domain. The acoustophoretic motion of the suspended particles of size a, is given by the radiation forces arising from the scattering of the incident waves on the particle calculated by Equation 5 and the Stokes drag force as a result of the steady acoustic streaming velocities (see Equation 8). A combination of both of these forces result in the net migration profile for a given particle size a.

4.2 Experimental setup

In order to validate the key numerical results, an experiment was conducted. The experiment consists of a 128° Y-cut X-propagating LN patterned with straight IDTs, corresponding to a SAW wavelength of $\lambda_{SAW} = 50 \mu$m. The rectangular microchannel containing the fluid has a width, $W = 500$ μm (i.e. 10 λ_{SAW}) and a height, $h = 50$ μm enclosed by PDMS walls, with the same aspect ratio for the channel dimensions relative to the wavelength as was used for the numerical study. An additional simulation was carried out to represent the experimental setup and added in the supplementary information (see ESI† Fig. S6). The wavelength, λ_{SAW} frequency, f channel dimensions (i.e. W and h) and decay coefficient, $C_d = 1590$ m^{-1} (calculated based on Equation 14) was altered accordingly to match the experimental parameters. To observe the size-dependence of acoustophoretic particle migration behaviour, two particle sizes were used, specifically $2a = 1.1$ μm and $2a = 5.1$ μm particles.

5 Results and discussion

5.1 Numerical model

5.1.1 Mesh convergence analysis

We carried out a mesh convergence analysis to confirm the spatial resolution is adequate to accurately capture the physics. Especially close to the viscous boundary layers which requires a very fine mesh. Owing to the rectangular nature of the channel cross-section, a distributed mapped mesh was utilised. The computational domain was separated into sections, namely, the channel side walls, the channel ceiling, the channel bottom (i.e. where the velocity boundary condition BC_{vel}, was imposed) and the bulk of the channel. Each of these sections, excluding the bulk of the channel were defined to have a 2 μm thick section spanning the corresponding width as shown in the Supplementay Information (see ESI† Fig. S7 (a)). The bulk mesh element size d_{bulk}, is restricted to have a maximum size corresponding to the size of the channel bottom, channel ceiling and channel side section. Initially, we set the boundary mesh element size, $d_b = 0.5$ μm × 0.02 μm and perform a mesh convergence analysis for a series of different parameters, by progressively decreasing d_b. The distribu-

tion of the mesh along with the convergence plot is plotted in the supplementary information (see ESI† Fig. S7). As a measure of convergence, we define a convergence function $C(g)$ for a solution g with respect to the reference solution g_{ref} (i.e. finest mesh distribution; $d_{b,finest} = 0.25$ μm × 0.01 μm) as used by Muller *et al*.[38]

$$C(g) = \sqrt{\frac{\int (g - g_{ref})^2 \, dx \, dy}{\int (g_{ref})^2 \, dx \, dy}} \tag{13}$$

In order to obtain a relative convergence of all the required parameters below $C(g) = 0.002$, we require a mesh size near the boundary of $d_b = 0.294$ μm × 0.0118 μm (i.e. $d_b/d_{b,finest} = 0.85$).

5.1.2 Boundary condition values: C_d and ζ

It is essential that the boundary conditions applied to the fluid domain model are an accurate representation of the fully coupled system. To that end, two values in Equation 12 need to be provided, these are C_d, the decay coefficient of the wave, and ζ, the relative amplitude of the x and y displacement components. We chose to determine C_d and ζ empirically, as follows.

From a fully coupled simulation, we extracted velocity components u_x and u_y along the interface. A least-squares fit of Equation 12 to the extracted velocity profiles then yielded $C_d = 2063$ m^{-1} and $\zeta = 0.86$ (see ESI† Fig. S1 and S2; ESI† Supplementary Movie S9 (Multimedia)). Note that the value for C_d agrees within just 3.8% of the theoretical SAW attenuation resulting from energy transfer from the substrate to the fluid domain, as given by[57]

$$C_d = \frac{\rho_0 c_0}{\rho_{LN} c_{LN} \lambda_{SAW}} \tag{14}$$

The same boundary condition (as in Equation 12) omitting the counter-propagating term can be used to model TSAW systems as well. The results of the analysis is included in the supplementary information (see ESI† Fig. S1 and S2).

5.1.3 Travelling wave component

Two opposing travelling waves of constant amplitude, frequency and wave number create a standing wave. In this case however, as a SAW couples into the fluid domain, it decays in amplitude resulting from the energy transfer into the fluid domain, corresponding to a decay length as given by Equation 14. As a result, we observe a combination of travelling and standing wave components throughout the channel width. The proportion of TSAW and SSAW varies spatially depending on the relative amplitudes of the two counter-propagating waves. The edges of the channel will have regions of larger travelling wave components (propagating towards the centre of the channel), whilst at the channel centre, standing wave components will dominate.

In the area in which the travelling wave component dominates (i.e. close to the channel walls), strong streaming rolls are present (Fig. 2 (c) and (d)). Whilst these streaming rolls have been observed previously in pure travelling wave systems (i.e.TSAW),[58,59] this is the first report of them in a SSAW system.

Fig 2 (a) shows a snapshot of the first order field at one moment in the oscillation cycle. It can be seen that there is a periodicity in both the x and y direction. When the magnitude of the pressure
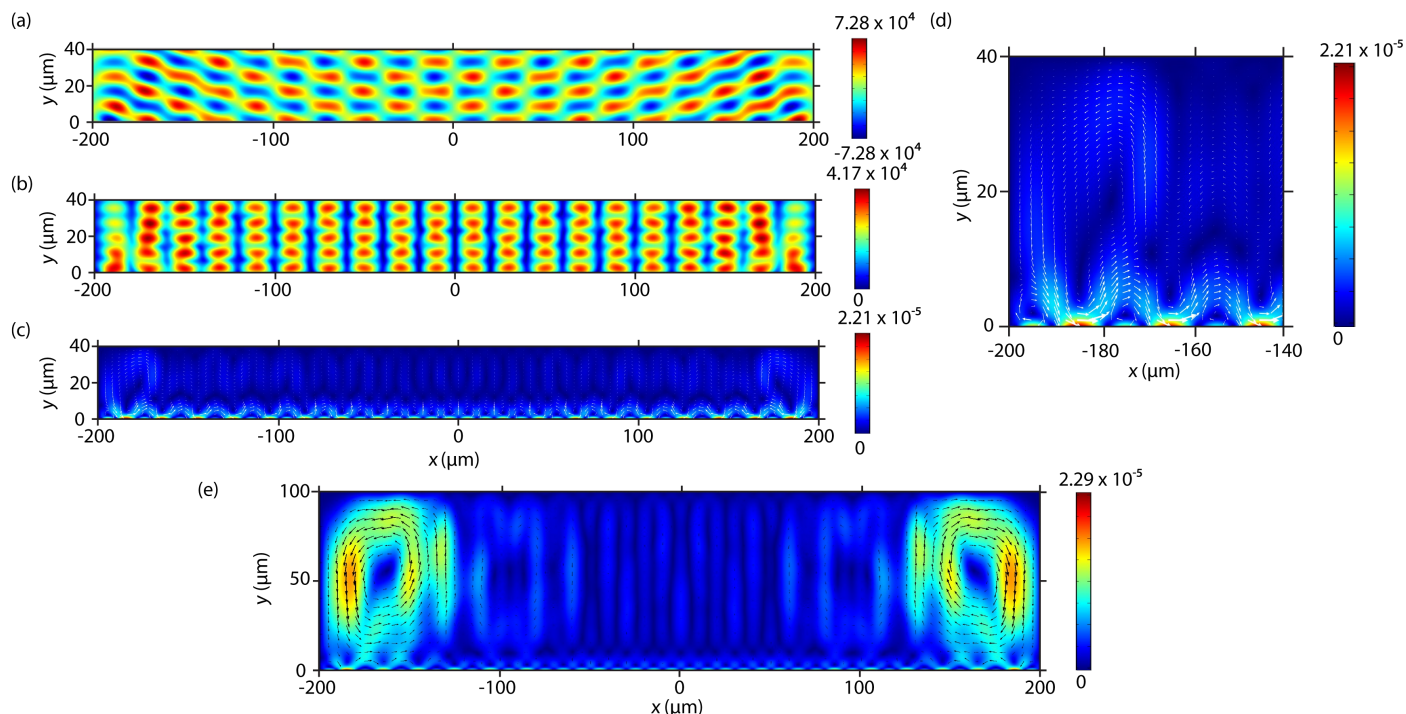
Fig. 2 Surface plots for a $W = 400$ μm (i.e. 10 λ_{SAW}) and $h = 400$ μm (i.e. λ_{SAW}) of the resultant (a) first-order pressure fields, P_1 (b) time-averaged modulus of the first-order pressure fields, $\langle|P_1|\rangle$ and (c) streaming velocity magnitude field $|v_2|$ overlaid with streaming velocity field vectors, $\boldsymbol{v}_2$ in white and (d) a zoomed in surface plots of the resultant streaming velocity magnitude field, $|v_2|$ overlaid with streaming velocity field vectors, $\boldsymbol{v}_2$ in white at the left hand side of the channel to illustrate the observed streaming rolls and (e) streaming velocity magnitude field $|v_2|$ overlaid with streaming velocity field vectors, $\boldsymbol{v}_2$ in black for a $h = 100$ μm (i.e. 2.5 λ_{SAW}). Pressure surface plots have units of Pa and velocity surface plot have units of m/s.

is plotted (i.e. removing phase information; Fig 2 (b)), it can be seen that in the y direction there is minimal spatial dependence because the vertically propagating component of the wave is partially reflected by the roof of the fluid cavity due to the impedance mismatch at the interface. In the x direction however, the sound field oscillates spatially between the red and blue extremes of the colour map in the centre of the channel, and that this fluctuation is not quite as well-defined away from the centre – indicative of a weaker standing wave component. This difference is rather subtle. A more striking feature is that the amplitude of the pressure field drops in the upper corners of each end of the channel. This is due to the travelling wave components, as the surface wave meets the edge of the fluid chamber, energy will couple into the fluid at the Rayleigh angle. However, in accordance to the Huygens-Fresnel principle and just as in the near-field of steered ultrasonic beam,[60] diffraction effects cause complicated pressure amplitude

patterns in the near-field consisting of a main and multiple side lobes. In this case the source of the acoustic beam is the excitation of the LN-fluid interface, previously observed in Collins *et al.*[61] Whilst, this effect is present throughout the channel width, it becomes less significant further away from the channel walls as a result of the inherent SAW decay. This effect is not as apparent in the pressure fields excited in SSAW systems as it is in TSAW systems (see ESI† Supplementary Movie S9 (Multimedia)). The attached multimedia clearly shows the formation of SSAW as well as the existence of the acoustic lobe pattern. It is this feature in the first order pressure field which gives rise to the rolls in the second order streaming field. In addition, at the top left and right-hand corners of Fig 2 (b-e), a time-averaged pressure local minima as well as a minimal effect imposed by the streaming velocity is observed. This accurately describes the underlying physics that gives rise to the presence of the anechoic corner as presented by Destgeer *et al.*[49]

Aside from the rolls at each end of the channel, the periodicity of the standing wave in the x direction gives rise to a second periodic feature in the streaming field. When the boundary layer is zoomed into, at the edge and centre of the channel, Fig 3, it can be seen that there is a steady decay in the streaming strength as the lower surface is approached. This is indicative of the streaming fields being driven by the velocity gradient within the resultant field itself (also known as Eckart streaming) this is in agreement with the one wavelength model done by Nama *et al.*[41] It can be seen from comparison of the streaming at the edge

Fig. 3 Zoomed in surface plots of the resultant streaming magnitude velocity field, $|v_2|$ at the viscous boundary layer (a) bottom left of the channel and (b) center of the channel. Surface plot have units m/s. Streaming velocity field vectors, $\boldsymbol{v}_2$ are depicted with black arrows and the red horizontal line marks the end of the viscous boundary layer, δ_v.
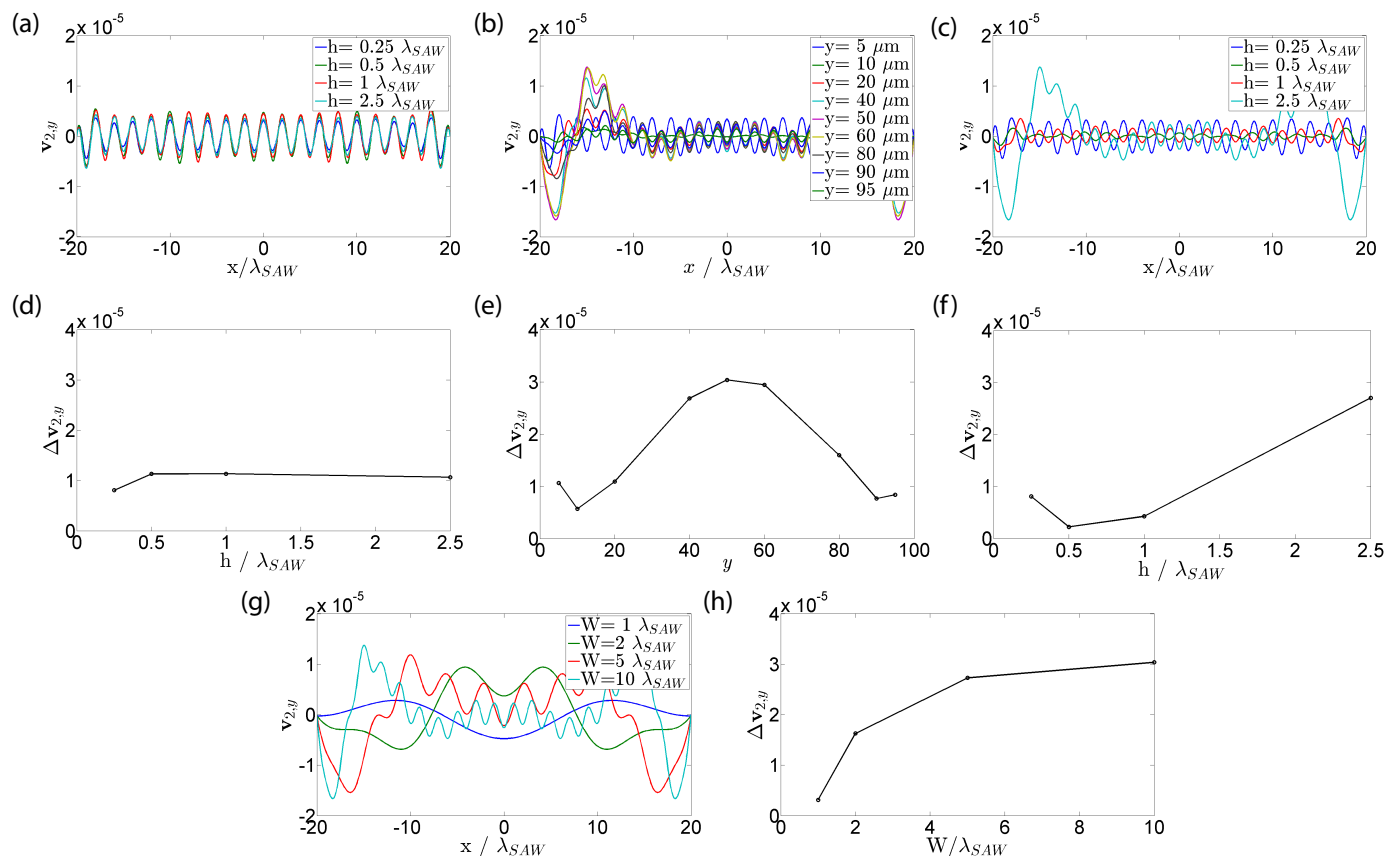
Fig. 4 Plot of the vertical streaming velocity, $v_{2,y}$ across the channel for varying channel heights h, at (a) $y = 5$ μm in a $W = 10$ λ_{SAW} channel, (b) plot of $v_{2,y}$ at different y locations in a $h = 2.5$ λ_{SAW}; $W = 10$ λ_{SAW} channel and (c) mid-height (i.e. $y = h/2$) in a $W = 10$ λ_{SAW} channel. Plot of $\Delta v_{2,y}$ against normalised channel height h/λ_{SAW} at (d) $y = 5$ μm in a $W = 10$ λ_{SAW} channel, (e) plot of $\Delta v_{2,y}$ against y in μm in a $h = 2.5$ λ_{SAW}; $W = 10$ λ_{SAW} channel and (f) plot of $\Delta v_{2,y}$ against normalised channel height h/λ_{SAW} $y = h/2$ in a $W = 10$ λ_{SAW} channel. (g) Vertical streaming velocity, $v_{2,y}$ and (h) streaming velocity strength $\Delta v_{2,y}$ plots across the channel for varying channel widths W against a normalised x position x/λ_{SAW}. All excitation wavelength $\lambda_{SAW} = 40$ μm and all $v_{2,y}$ units in m/s. See ESI† Fig. S3, S4 and S5 for corresponding streaming velocity surface plots. Note: Plots (a-c) and (g) are symmetrical about $x/\lambda_{SAW} = 0$.

and middle of the chamber that there is little alteration across the width of the chamber in the forces driving this spatially periodic part of the streaming field.

5.1.4 The effect of height

In BAW actuated systems, the standing wave consists of waves bouncing between the end walls of the chamber, as such they are propagating parallel to the upper and lower surface of the channel. Hence the particle velocity varies strongly in the vicinity of these non-slip boudnaries. Muller *et al* showed that the streaming in the bulk of the fluid is predominantly driven by the boundary layer streaming (also known as Schlichting streaming), therefore the strength of the dominant streaming field (i.e. close to the top and bottom of the channel) was independent of the height of the channel.[38] In contrast, waves in a SAW system propagate at an angle to all surfaces, so Schlichting streaming appears to play less of a role. Instead, we have shown that there are two features in the streaming field, one due to the lobes at the ends of the channel, and the other due to gradients in the pressure field. Now we will examine how the strength of each of these varies with channel height.

Firstly, comparing the streaming fields in Fig 2 (c) and (e), it

can be seen visually that the streaming rolls become much larger and stronger in higher channels and seemingly much more significant than the periodic streaming. To test this, we consider the streaming at the bottom of the channel and in the middle of the channel separately. In Fig 4(a) the streaming velocity $v_{2,y}$ and streaming strength $\Delta v_{2,y}$ (i.e. calculated as the difference between the maximum upwards (positive $v_{2,y}$) vertical velocity and the maximum downward (negative $v_{2,y}$) vertical velocity) in the vertical direction, is plotted at $y = 5$ μm for channels of four different heights h. It can be seen that there is very modest variation in amplitude of the streaming at this height, dominated as it is by the periodic streaming pattern. At locations higher than this in the channel, however, the streaming rolls at each end of the channel become more significant. Firstly, this is shown by plotting $v_{2,y}$ at different heights within a 2.5 λ_{SAW} channel, Fig 4 (b) and (e). It can be seen that change in the vertical streaming velocity $\Delta v_{2,y}$, indicating the strength of a swirling flow, is significantly higher at the mid-height of the channel (i.e. $y = h/2$), especially at the edges due to the streaming rolls. By plotting the mid-height $v_{2,y}$ for a range of channel heights Fig. 4 (c) it can be seen that when the rolls are present, above a height of $\lambda_{SAW}/2$, the rolls become much greater in strength with increasing height h, Fig. 4 (f), and

with increased width W (Fig. 4 (g) and (h)).

As the height, h of the channel increases, the acoustic wave propagating within the fluid medium attenuates more as the propagation distance increases. Therefore, the effects of streaming especially close to the channel walls becomes more dominant and apparent, leading to a spatial dependence of acoustophoretic particle migration. In Fig. 4(h), the streaming velocities $\Delta \boldsymbol{v}_{2,y}$ against the normalised channel widths, W/λ_{SAW} along a line of $y = h/2$ is plotted. We observe as W increases, the effects of streaming dominated by the rolls at the channel walls increase in strength. This is a direct result of the increase in the travelling wave component as the channel width increases - as such it clearly shows the need for accurately including the travelling wave decay in the boundary conditions.

Through the development of boundary conditions which are applicable to channels of widths greater than λ_{SAW} and as such relevant to most type of SAW acoustofluidics systems, we have been able to characterise the streaming as being dominated by two features; streaming rolls at the ends of the channels and a periodic structured streaming field. It is clear that the relative importance of these is height dependant across different geometry channels, and spatially dependent within any one channel (the rolls being a local effect), neither of which are observed in BAW systems.

5.1.5 Particle trajectories

Suspended particles are exposed to two key forcing mechanisms in acoustofluidics systems, the acoustic radiation force which acts directly on the particle, and the drag forces arising via the acoustic streaming flow field. The former, which acts to collect the particles, scales with a power relationship with respect to a (provided $a \ll \lambda_{SAW}$) (i.e. $F_{SW} \propto a^3$ [62] and $F_{TW} \propto a^6$ [47]). The latter acts to swirl the particles around looping trajectories, scales linearly (Equation 8). This difference in power relationship means that the dominant force will be size dependant, with ARF becoming more important for larger particle sizes. Hence, a cut-off size exists, above which particles will be collected (ARF dominated) and below which the particles will swirl (i.e. streaming domi-
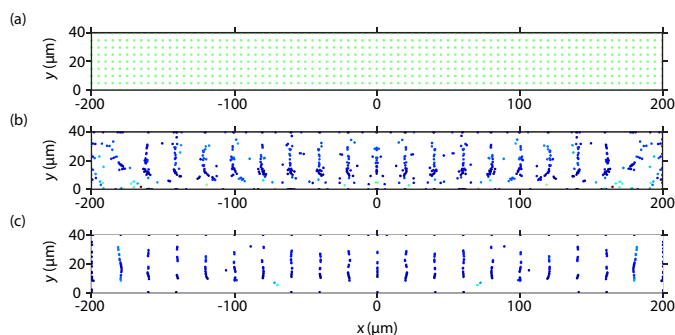
Fig. 5 Particle locations within a 40 μm high chamber (i.e. λ_{SAW}). (a) Initially, particles are distributed uniformly within the microchannel. particle end location at $t_{end} = 5$ s for given diameters $2a$ of (b) 1 μm (Particle velocity ranges from 0 μm/s (dark blue) to 7.4 μm/s (dark red)) and (c) 2 μm (particle velocity ranges from 0 μm/s (dark blue) to 10 μm/s (dark red)). ESI† Supplementary Movie S10 (Multimedia).
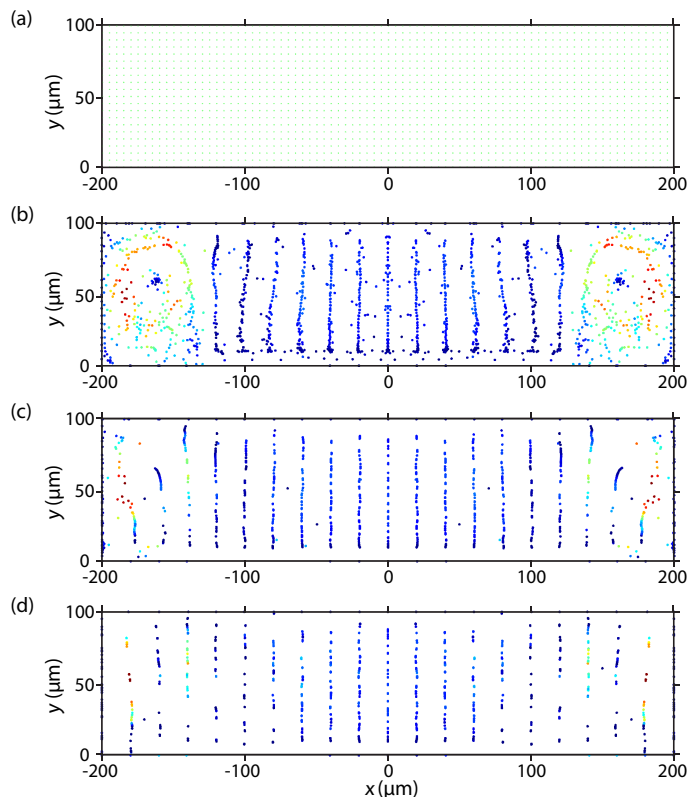
Fig. 6 Particle trajectory within a 100 μm high chamber (i.e. 2.5 λ_{SAW}). (a) Initially, particles are distributed uniformly within the microchannel. Particle end location for given particle diameters $2a$ of (b) 1 μm ($t_{end} = 5$ s; particle velocity ranges from 0 μm/s (dark blue) to 17.3 μm/s (dark red)), (c) 2 μm ($t_{end} = 5$ s; particle velocity ranges from 0 μm/s (dark blue) to 17.4 μm/s (dark red)) and (d) 4 μm ($t_{end} = 4$ s; particle velocity ranges from 0 μm/s (dark blue) to 16.4 μm/s (dark red)). ESI† Supplementary Movie S11 (Multimedia)

nated). In BAW systems, the streaming in the bulk of the fluid predominantly is driven by boundary layer streaming, a single cut-off size was obtainable without geometric dependence (over a certain range of realistic channel sizes).[38] In the case of SAW however, we have demonstrated a geometric and spatial dependence in the streaming field. The effect this has on the cut-off size will now be examined.

Having obtained the second-order pressure fields and the steady streaming fields, we introduce particles of a given size a and analyse their trajectories over a full range of initial locations. As shown in Fig. 5 (see ESI† Supplementary Movie S10 (Multimedia)) and 6 ((see ESI† Supplementary Movie S11 (Multimedia))) we observe a spatial dependence across the channel of dominant forcing mechanism (i.e. either ARF or streaming induced drag forces) for a given particle size. This is a direct result of the streaming rolls close the channel walls. For a given particle size of $2a = 1$ μm and $2a = 2$ μm in a $h = 100$ μm channel, we observe a streaming dominant behaviour close to the channel walls and ARF dominant behaviour in the central region of the channel (see Fig. 6(b) and (c); ESI† Supplementary Movie S11 (Multimedia)). However, if the particle size is increased to $2a = 4$ μm, we only observe an ARF dominant forcing behaviour throughout the channel

width (see Fig. 6 (d); ESI† Supplementary Movie S11 (Multimedia)). Hence for particle collection across the whole channel, an increase in particle size is required to suppress the effects of the strongest streaming dominant region. As these spatially dependant rolls become stronger with larger channel heights this also increases the cut-off size to achieve particle collection throughout the channel width.

Equation 5 is valid within the Rayleigh limit, approximately $a < \lambda_f/10$, within this limit we see a transition from particles dominated by streaming induced drag forces to standing wave driven acoustic radiation forces as the particle size is increased. However, as has been previously described, with further increase in particle size there will also be a transition from behaviour dominated by standing waves to that dominated by acoustic radiation forces generated by the travelling wave component. This second transition was demonstrated, using a 2D model with numerically calculated forces. For particles with $a/\lambda_f = 1/6$ in a field with a SW/TW amplitude ratio ≈ 0.3.[42] The minimum SW/TW ratio in the work presented here is ≈ 0.8 (see ESI† Fig. S8). As such, this transition occurs well beyond the limit of Equation 5. The SW/TW ratio can be further reduced to observe dominance of the radiation forces arising from the travelling wave component in the fluid domain by utilising an asymmetrical signal amplitude as previously performed by Devendran *et al.*[42]

5.2 Experimental particle migration

The experiment performed to validate the key features observed with particle migration behaviour, consisted of loading of $2a = 1.1$ µm and $2a = 5.1$ µm particles into the device separately as described in Section 4.2. It should be noted that the experimental setup consisted of a $\lambda_{SAW} = 50$ µm IDT finger pair. Numerical results representing this experimental scenario are presented in the Supplementary Information (see ESI† Fig. S6) and returned a similar, albeit relatively less pronounced streaming roll at the channel wall. A SSAW field was established within the channel and for the case of $2a = 1.1$ µm particles, the majority of par-

ticles were observed to migrate to the nearest pressure node as viewed from the top of the channel. At the edges of the channel a strong streaming roll developed with particles recirculating close to the channel walls as predicted by the particle trajectory model (see Fig. 5 (b) and 6 (b)). As shown in Fig. 7 (a), we see a spatial dominance of particle migration behaviour, whereby, the channel edges do not observe strong collection lines (particle recirculate in these regions; $x = -250$ µm to -200 µm and $x = 200$ µm to 250 µm) as opposed to distinct particle collection at the centre of the channel. Particles within this roll were observed to move upwards, then towards the wall, downwards and then back to their starting position as clearly depicted in the supplementary video (ESI† Supplementary Movie S12 (Multimedia)). In contrast, when the particle size is increased to $2a = 5.1$ µm as shown in Fig. 7 (b), we observe distinct particle collection lines all throughout the channel width as predicted by the particle trajectory models in Fig. 5 (c) and 6 (d).
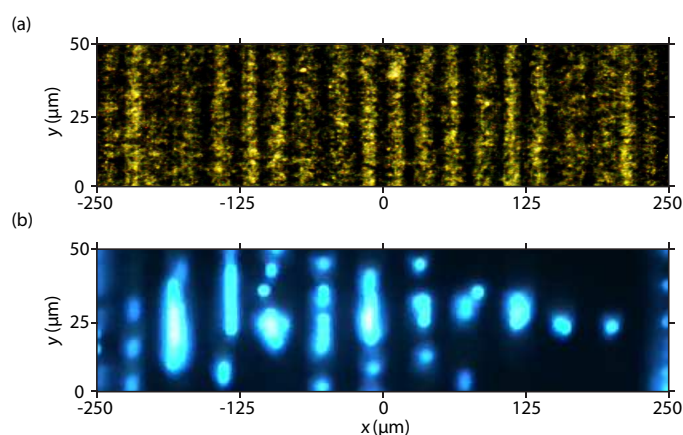
6 Conclusions

We report a numerical approach using finite element analysis via COMSOL Multiphysics to accurately predict the acoustophoretic motion of suspended particles within a microchannel. To circumvent the need to model a computationally expensive fully coupled piezoelectric-fluid system, we use boundary condition which correctly capture the travelling and standing wave components of the surface waves, this enables the omission of the piezoelectric domain. The proposed boundary condition was tested against numerous fully coupled piezoelectric-fluid systems and resulted in very good agreement. Key to the finding is the consideration of the inherent travelling wave component, specifically its effect on the acoustic streaming field which results in relatively strong rolls near the channel side walls when the channel spans multiple wavelengths, λ_{SAW}. These streaming rolls are driven by the nature of SAW based acoustofluidics systems that observe an attenuation of the upwards propagating acoustic wave towards the channel ceiling at the Rayleigh angle. In contrast to BAW systems, whereby, the bulk streaming field is driven by the boundary layer streaming (i.e. Schlichting streaming), streaming fields within SAW systems are driven by the velocity gradient resulting from the attenuation within the fluid. Thus, it is shown that as the height of the channel increases, the strength of these streaming rolls increase in contrast to that observed within BAW systems. As a result we find a size-dependent acoustophoretic migration of particles that consist of a width-wise spatial variation in dominant forcing mechanisms. These numerical results and predictions have been validated experimentally to show the key streaming features observed in typical SSAW based microfluidic systems.

7 Acknowledgements

Fig. 7 Experimental results showing different acoustophoretic particle migration behaviour as seen from a top view of (a) $2a = 1.1$ µm and (b) $2a = 5.1$ µm particle size within a $\lambda_{SAW} = 50$ µm, $W = 10$ λ_{SAW} and $h = \lambda_{SAW}$ system. ESI† Supplementary Movie S12 (Multimedia)

Lab on a Chip Accepted Manuscript

References

1 J. Gardeniers and A. Van den Berg, *Analytical and Bioanalytical Chemistry*, 2004, **378**, 1700–1703.

2 J. McGrath, M. Jimenez and H. Bridle, *Lab on a Chip*, 2014, **14**, 4139–4158.

3 M. Yamada, M. Nakashima and M. Seki, *Analytical Chemistry*, 2004, **76**, 5465–5471.

4 N. Xia, T. P. Hunt, B. T. Mayers, E. Alsberg, G. M. Whitesides, R. M. Westervelt and D. E. Ingber, *Biomedical Microdevices*, 2006, **8**, 299–308.

5 Y. Wang, Y. Zhao and S. K. Cho, *Journal of Micromechanics and Microengineering*, 2007, **17**, 2148.

6 M. MacDonald, G. Spalding and K. Dholakia, *Nature*, 2003, **426**, 421–424.

7 B. Landenberger, H. Höfemann, S. Wadle and A. Rohrbach, *Lab Chip*, 2012, **12**, 3177–3183.

8 P. R. Gascoyne and J. Vykoukal, *Electrophoresis*, 2002, **23**, 1973.

9 H. Shafiee, M. B. Sano, E. A. Henslee, J. L. Caldwell and R. V. Davalos, *Lab Chip*, 2010, **10**, 438–445.

10 M. Hill, R. J. Townsend and N. R. Harris, *Ultrasonics*, 2008, **48**, 521–528.

11 I. Leibacher, P. Reichert and J. Dual, *Lab Chip*, 2015, **15**, 2896–2905.

12 L. Schmid, D. A. Weitz and T. Franke, *Lab Chip*, 2014, **14**, 3710–3718.

13 H. Bruus, J. Dual, J. Hawkes, M. Hill, T. Laurell, J. Nilsson, S. Radel, S. Sadhal and M. Wiklund, *Lab Chip*, 2011, **11**, 3579–3580.

14 M. Gedge and M. Hill, *Lab Chip*, 2012, **12**, 2998–3007.

15 L. Y. Yeo and J. R. Friend, *Biomicrofluidics*, 2009, **3**, 012002.

16 J. Hultström, O. Manneberg, K. Dopf, H. M. Hertz, H. Brismar and M. Wiklund, *Ultrasound in Medicine and Biology*, 2007, **33**, 145–151.

17 D. Bazou, R. Kearney, F. Mansergh, C. Bourdon, J. Farrar and M. Wride, *Ultrasound in Medicine and Biology*, 2011, **37**, 321–330.

18 D. J. Collins, B. Morahan, J. Garcia-Bustos, C. Doerig, M. Plebanski and A. Neild, *Nature Communications*, 2015, **6**, year.

19 A. Neild, S. Oberti, F. Beyeler, J. Dual and B. J. Nelson, *Journal of Micromechanics and Microengineering*, 2006, **16**, 1562.

20 A. Haake, A. Neild, G. Radziwill and J. Dual, *Biotechnology and Bioengineering*, 2005, **92**, 8–14.

21 M. Hill, Y. Shen and J. J. Hawkes, *Ultrasonics*, 2002, **40**, 385–392.

22 M. Hill and R. J. Wood, *Ultrasonics*, 2000, **38**, 662–665.

23 V. Skowronek, R. W. Rambach, L. Schmid, K. Haase and T. Franke, *Analytical Chemistry*, 2013, **85**, 9955–9959.

24 D. J. Collins, T. Alan, K. Helmerson and A. Neild, *Lab Chip*, 2013, **13**, 3225–3231.

25 M. Sesen, T. Alan and A. Neild, *Lab Chip*, 2015, **15**, 3030–3038.

26 L. R. Huang, E. C. Cox, R. H. Austin and J. C. Sturm, *Science*, 2004, **304**, 987–990.

27 J. Shi, D. Ahmed, X. Mao, S.-C. S. Lin, A. Lawit and T. J. Huang, *Lab Chip*, 2009, **9**, 2890–2895.

28 A. Fakhfouri, C. Devendran, D. J. Collins, Y. Ai and A. Neild, *Lab Chip*, 2016, **16**, 3515–3523.

29 A. Bernassau, C. Courtney, J. Beeley, B. Drinkwater and D. Cumming, *Applied Physics Letters*, 2013, **102**, 164101.

30 C. Devendran, D. R. Billson, D. A. Hutchins and A. Neild, *Sensors and Actuators B: Chemical*, 2016, **224**, 529 – 538.

31 H. Li, J. R. Friend and L. Y. Yeo, *Biomedical Microdevices*, 2007, **9**, 647–656.

32 R. Shilton, M. K. Tan, L. Y. Yeo and J. R. Friend, *Journal of Applied Physics*, 2008, **104**, 014910.

33 H. V. Phan, T. Alan and A. Neild, *Analytical chemistry*, 2016.

34 C. Devendran, I. Gralinski and A. Neild, *Microfluidics and Nanofluidics*, 2014, **17**, 879–890.

35 P. Rogers, I. Gralinski, C. Galtry and A. Neild, *Microfluidics and Nanofluidics*, 2013, **14**, 469–477.

36 A. Neild, S. Oberti, A. Haake and J. Dual, *Ultrasonics*, 2006, **44**, 455–460.

37 J. Dual, P. Hahn, I. Leibacher, D. Möller, T. Schwarz and J. Wang, *Lab Chip*, 2012, **12**, 4010–4021.

38 P. B. Muller, R. Barnkob, M. J. H. Jensen and H. Bruus, *Lab Chip*, 2012, **12**, 4617–4627.

39 J. Lei, P. Glynne-Jones and M. Hill, *Lab Chip*, 2013, **13**, 2133–2143.

40 P. B. Muller, M. Rossi, A. Marin, R. Barnkob, P. Augustsson, T. Laurell, C. J. Kaehler and H. Bruus, *Physical Review E*, 2013, **88**, 023006.

41 N. Nama, R. Barnkob, Z. Mao, C. J. Kähler, F. Costanzo and T. J. Huang, *Lab Chip*, 2015, **15**, 2700–2709.

42 C. Devendran, N. R. Gunasekara, D. J. Collins and A. Neild, *RSC Advances*, 2016, **6**, 5856–5864.

43 D. J. Collins, T. Alan and A. Neild, *Lab Chip*, 2014, **14**, 1595–1603.

44 Y. Chen, A. A. Nawaz, Y. Zhao, P.-H. Huang, J. P. McCoy, S. J. Levine, L. Wang and T. J. Huang, *Lab Chip*, 2014, **14**, 916–923.

45 X. Ding, S.-C. S. Lin, M. I. Lapsley, S. Li, X. Guo, C. Y. Chan, I.-K. Chiang, L. Wang, J. P. McCoy and T. J. Huang, *Lab Chip*, 2012, **12**, 4228–4231.

46 G. Destgeer, B. H. Ha, J. H. Jung and H. J. Sung, *Lab Chip*, 2014, **14**, 4665–4672.

47 G. Destgeer, K. H. Lee, J. H. Jung, A. Alazzam and H. J. Sung, *Lab Chip*, 2013, **13**, 4210–4216.

48 H. Bruus, *Lab Chip*, 2012, **12**, 20–28.

49 G. Destgeer, B. H. Ha, J. Park, J. H. Jung, A. Alazzam and H. J. Sung, *Analytical Chemistry*, 2015, **87**, 4627–4632.

50 M. Settnes and H. Bruus, *Physical Review E*, 2012, **85**, 016327.

51 W. Nyborg, *Physical Acoustics*, 1965, **2**, 265.

52 S. Shiokawa, Y. Matsui and T. Ueda, Ultrasonics Symposium, 1989. Proceedings., IEEE 1989, 1989, pp. 643–646.

53 J. Lighthill, *Journal of Sound and Vibration*, 1978, **61**, 391–418.

Lab on a Chip Accepted Manuscript

54 D. Köster, *SIAM Journal on Scientific Computing*, 2007, **29**, 2352–2380.

55 W. M. Haynes, *CRC handbook of chemistry and physics*, CRC press, 2014.

56 J. K. Tsou, J. Liu, A. I. Barakat and M. F. Insana, *Ultrasound in Medicine & Biology*, 2008, **34**, 963 – 972.

57 M. B. Dentry, L. Y. Yeo and J. R. Friend, *Physical Review E*, 2014, **89**, 013203.

58 J. Vanneste and O. Bühler, Proceedings of the Royal Society of London A: Mathematical, Physical and Engineering Sciences, 2011, pp. 1779–1800.

59 A. Sonato, M. Agostini, G. Ruffato, E. Gazzola, D. Liuni, G. Greco, M. Travagliati, M. Cecchini and F. Romanato, *Lab on a Chip*, 2016, **16**, 1224–1233.

60 S.-C. Wooh and Y. Shi, *Journal of nondestructive evaluation*, 1999, **18**, 39–57.

61 D. J. Collins, C. Devendran, Z. Ma, J. W. Ng, A. Neild and Y. Ai, *Science Advances*, 2016, **2(7)**, e1600089.

62 L. Gorkov, *Soviet Physics Doklady*, 1962, **6**, 773–775.